

# MJO structure associated with the higher-order CEOF modes

Ping Liu

Received: 27 June 2013 / Accepted: 2 December 2013 / Published online: 3 January 2014  
© Springer-Verlag Berlin Heidelberg 2013

**Abstract** The real-time multivariate Madden–Julian oscillation (RMM; MJO) index has been widely employed to monitor the amplitude, phase, and time evolution of MJO events, as the index is formulated from the leading two combined-empirical orthogonal function (CEOF) modes of daily anomalous OLR and 850- and 200-hPa zonal winds, and the modes describe the MJO dynamics well. These two CEOF modes, however, are known to dominate in power spectra at zonal wavenumber one and may underestimate the power and structure at wavenumbers 2–5 where many MJO events are also prominent. This study approximated a baseline for MJO by applying band-pass filters to daily anomalies on 30–100 day periods and at 1–5 eastward propagating waves, as slightly different bands led to the same conclusions. Following the procedures to develop the RMM index, the daily anomalous data were derived and subjected to the CEOF analysis with all modes archived for diagnosis. Different numbers of the leading modes were compared in explained variance, standard deviation (STD), and wavenumber power spectra to describe the overall MJO magnitude and structure, and on the Hovmöller diagrams to represent the evolution of three distinct MJO events. Results show that the two leading CEOF modes explain only a small portion of the power spectra at wavenumbers 2–5. This spectral leakage notably reduces the MJO amplitude, particularly of the OLR in the western Pacific. The CEOF modes 3–10 can withhold power sufficiently such that the anomalies reconstructed by the first 10 modes contribute most of the

baseline variance; their structures agree well with the baseline by constituting nearly the same proportion in the region from the central Indian Ocean to the dateline and by providing more complete evolutions of the three MJO events on the Hovmöller diagrams. Meanwhile, these modes introduce a notable amount of power for the equatorial Rossby and Kelvin waves that are partially embedded in the evolution of MJO. The first 50 of the total 432 CEOF modes retain all variance of the baseline MJO, while those higher than 10 contain less information and more noise and can be discarded. Furthermore, this study indicated that the longitudinal STD of the reconstructed anomalies detects the MJO phases and magnitudes in the western Pacific with more physical meaning and in better agreement with the Hovmöller diagrams than the RMM-like amplitude. The results provide an integral figure of the MJO structure from the CEOF analysis and a more robust RMM framework for monitoring the MJO's evolution in real time and for validating its numerical forecast and simulations.

**Keywords** MJO · RMM index · CEOF

## 1 Introduction

A wide range of frequencies and zonal wavenumbers are associated with the Madden–Julian oscillation (MJO; Madden and Julian 1971, 1972), which is a dominant but episodic mode of the tropical intraseasonal variability. The bands including 30–100 day periods and zonal wavenumbers 1–5 of eastward propagation were used to characterize the MJO in several widely referenced studies (Wheeler and Kiladis 1999), although a consensus of the bands for the MJO remains elusive (Straub 2013). This study chooses these bands to loosely set the baseline of the MJO for a

---

P. Liu (✉)  
School of Marine and Atmospheric Sciences (SoMAS),  
Stony Brook University, 199 Endeavour Hall, Stony Brook,  
NY 11794-5000, USA  
e-mail: Ping.Liu@stonybrook.edu

better comparison with prior investigations (Wheeler and Hendon 2004), and because slightly different ranges (Hendon and Salby 1994; Maloney and Hartmann 1998; Hendon et al. 1999; Kiladis et al. 2005) lead to similar results.

The MJO is a closely coupled mode of anomalies in convection and zonal winds. In a composite lifecycle of tens of MJO events (Hendon and Salby 1994), positive convection is initiated in the western Indian Ocean, develops and matures in the eastern Indian Ocean, weakens somewhat over the Maritime Continent, strengthens again in the western Pacific, and finally diminishes near the dateline. Correspondingly, the wind anomalies are out of phase in the lower and upper troposphere but in quadrature with the convection by  $90^\circ$  in phase. The coupled pattern in convection and circulation propagates eastward coherently in the above characteristic bands. Nevertheless, locations of anomaly centers can be different from those composited to form distinct zonal width and periods for each event (Straub 2013).

Many indices have been designed to represent the evolution and structure of the MJO (Lau and Chan 1985; Knutson and Weickmann 1987; and others). Straub (2013) categorized the existing indices into (1) cloudiness-based, (2) dynamical- or circulation-based, and (3) combined cloudiness- and dynamical-based types according to the data used. A few of them are also based on the method summarized here, while the rest are referred to Straub (2013) and the original references therein for more discussion. Slingo et al. (1996, 1999) selected the zonal mean zonal wind at 200 hPa subject to 20–100-day band-pass filtering and 101-day running mean to describe the overall MJO activity in the troposphere, particularly at interannual time scales. Sperber (2003) used this index to describe the vertical structure of the MJO. Maloney and Hartmann (1998) applied the empirical orthogonal function (EOF) analysis to the 20–80-day filtered 850-hPa zonal wind so as to form an MJO index and construct the composite MJO life cycle. However, most of the indices are based on one or two fields and cannot directly disclose the convection-circulation coupled features of the MJO. Moreover, conventional band-pass filtering produces large bias near the edge of the data sets, making the indices less suitable for real-time applications.

Wheeler and Hendon (2004; WH04 hereafter) developed a unique real-time multivariate MJO (RMM) index without using band-pass filtering. They formulated the index with OLR as a proxy of convection and the 850- and 200-hPa zonal winds subject to delicate treatment detailed in the next section. They removed the seasonal cycle, trend, and interannual-decadal variations from the daily fields using harmonics, regressions, and subtraction of retrospective 120-day means. Finally, they averaged the fields

in  $15^\circ\text{S}$ – $15^\circ\text{N}$  to reduce the variance of high-frequency waves. The resulting anomalous time series retain the greatest variance at MJO scales; they are then subjected to combined EOF (CEOF) analysis to further suppress noise. The RMM indices, equivalent to the principal components (PCs), are finally derived by projecting the anomalous time series onto the first two CEOF modes. Because the two RMMs are mutually orthogonal and disclose the evolution of the two dominant modes in lead and lag by some 10 days, they form a unique phase map that divides an MJO into eight phases at different geographical locations in the tropics. On the map, the RMM coordinates rotate counterclockwise as the MJO propagates eastward; an MJO phase is identified when the RMM's coordinates move outside of the unit circle, although some MJO phases can still be located inside (e.g., Straub 2013). This eight-octant map thus tracks the geographical evolution of pronounced MJO phases in real time (e.g., Straub 2013). The RMM amplitude, defined as  $(\text{RMM1}^2 + \text{RMM2}^2)^{1/2}$ , is used to represent the overall magnitude of MJO activity. In combination with the RMM index, the anomalous OLR is usually reconstructed as the benchmark to represent the evolution of MJO anomalies in amplitude and structure (WH04). Because the edge effect from the conventional band-pass filtering is excluded, the RMM index has been employed by operational centers to monitor real-time MJO evolution (e.g., Gottschalck et al. 2010) and by the modeling community in validating the MJO forecast and simulations (e.g., Liu et al. 2009).

WH04 indicated that the third CEOF mode contains MJO power spectra less prominent than the first two; this and the rest of the modes are discarded in the representation of the MJO. Nevertheless, the first two CEOFs explain only 26 % of the total variance (WH04). Such a small contribution suggests (1) the possibility of a large MJO residual in the rest of the CEOF modes, and that (2) the anomalies reconstructed by the RMM modes may not sufficiently retain the MJO structure, because the first two modes are predominant at zonal wavenumber 1 (Sect. 3) and because an MJO event can be different in zonal width or locations of convection centers from those that are well described by the leading two modes. The lost MJO variance particularly at zonal wavenumbers 2–5 must occur in higher-order CEOF modes. Since the RMM has become the standard MJO index (Straub 2013), it is of great importance to make it as robust as possible. These issues motivate the present study to investigate (1) how the higher-order CEOF modes contribute to the MJO power spectra and structure at zonal wavenumbers 2–5, (2) what other signal and noise must be included if the MJO at these wavenumbers are to be retained sufficiently, and (3) whether the additional CEOF modes can make the MJO detection more accurate with the extra non-MJO variance.

Section 2 reviews the steps to derive the anomalous data of WH04 and the methods for analysis. Section 3 compares the MJO power spectra and structure with those reconstructed by the RMM modes by including the higher-order CEOF modes to show that the first ten modes retain the MJO structure sufficiently; they contribute to the total MJO variance in the same proportion in the region from the central Indian Ocean to the dateline, and retain the evolutions of three distinct MJO events observed during the Tropical Ocean Global Atmosphere Coupled Ocean Atmosphere Response Experiment (TOGA-COARE; Webster and Lukas 1992) and spring 2012. Section 4 gives summary and discussion and concludes with an improved RMM framework.

## 2 The anomalous data and methods

The procedures in WH04 were followed closely to construct the daily anomalous time series using the OLR from the satellite measurements of the National Oceanic and Atmospheric Administration (NOAA; Liebmann and Smith 1996) and the 850- and 200-hPa zonal winds (U850 and U200 hereafter) produced by the NCEP/NCAR Reanalysis project (Kalnay et al. 1996). The daily data are globally distributed at  $2.5^\circ \times 2.5^\circ$  in latitude and longitude and cover 1 January 1979 through 31 December 2012, while the subset until the end of 2001 was used for the CEOF analysis. Their seasonal cycle consists of the time mean and the first three harmonics of the annual cycle during 1979–2001. The interannual variation is associated with the first rotated EOF (REOF) mode of the SST in  $55^\circ\text{S}$ – $60^\circ\text{N}$  and  $30^\circ\text{E}$ – $70^\circ\text{W}$  (Drosowsky and Chambers 2001; WH04), where the monthly SST in 1950–2012 was derived from the Hadley Centre Sea Ice and Sea Surface Temperature data set (HadISST; Rayner et al. 2003). Before the EOF analysis, the SST data were standardized and detrended in time, and then interpolated from  $1^\circ \times 1^\circ$  to  $5 \times 5^\circ$  using a box average. Consistent with WH04, the EOF analysis was applied to the subset of 1950–1993 and the REOF (NCAR 2013) to the first two modes, which is slightly different from the results of more recent subsets. The first principal component from the REOF (PC1 or SST1) was linearly interpolated over a monthly to daily interval and subjected to a 120-day-centered running mean to smooth the transition between adjacent months. The anomalies were then regressed onto the SST1 to produce parameters for each month, and the parameters interpolated linearly to each day as the interannual variation. Besides the seasonal cycle and the regressions, more interannual signal, trend, and variations of even lower frequency were removed sufficiently by subtracting the retrospective 120-day means. Finally, the average of the anomalies in

$15^\circ\text{S}$  and  $15^\circ\text{N}$  forms the anomalous fields of WH04, which are termed as raw anomalous data below.

Before the CEOF analysis (Kim et al. 2009) on the covariance matrix (WH04), the anomalous time series on each grid point was normalized by the global standard deviation (STD averaged in all longitudes) of the corresponding field so that each variable represents the same amount of variance to the analysis. All 432 CEOF modes were archived for comparison. After the CEOF, the global STDs were scaled back to the reconstructed anomalous time series to compare with the original data sets. The RMM index was constructed by projecting the anomalous data onto the first two CEOF modes and standardizing in time. The RMM modes of WH04 are provided as reference (available at <http://cawcr.gov.au/staff/mwheeler/maproom/RMM/>).

The MJOs of the raw anomalous time series and of those reconstructed from different numbers of CEOF modes were approximated in 30–100 day periods and at zonal wavenumbers 1–5 of eastward propagation using the band-pass filtering program of Wheeler and Kiladis (1999; WK99 hereafter). This filtering gives anomalies presumably too smooth to represent the precise MJO initiation (Straub 2013). Also following WK99, the equatorial Rossby (ER) waves were filtered at the bands of 6–50 days and wavenumbers 1–10 in westward propagation, and the equatorial Kelvin waves filtered at 2.5–30 days and wavenumbers 1–14 in eastward propagation, although Roundy (2012a, b) highlighted that this band includes some of the zonally narrow, slow MJO-like features as well. Successive 180-day overlapping subsets were used for computing frequency-wavenumber power spectra, for which the band-pass filtered anomalies in the first and last 120 days, long enough by test to eliminate the edge effect, were excluded.

## 3 Results

### 3.1 Power spectra of raw anomalous fields

The raw anomalous time series retain power spectra primarily for the MJO, which is shown in Fig. 1 as the basis for comparison. The OLR (Fig. 1a) is clearly dominant in eastward propagation at wavenumbers 1–5 and periods of 30–100 days. The spectral center is located at wavenumber 1 and near 60 days with a value slightly larger than  $1.4 \text{ W}^2 \text{ m}^{-4}$ . Notably, the power is reduced only slightly—by about  $1.3 \text{ W}^2 \text{ m}^{-4}$ —at wavenumber 2 and around 50–60 days. It decays to  $0.7 \text{ W}^2 \text{ m}^{-4}$  (about half) at wavenumber 3 and drops rapidly beyond. The U850 (Fig. 1b) has power spectra also strongest at wavenumber 1 and around 45–60 days. The central value is slightly larger than  $0.08 \text{ m}^2 \text{ s}^{-2}$ , while the power decays to

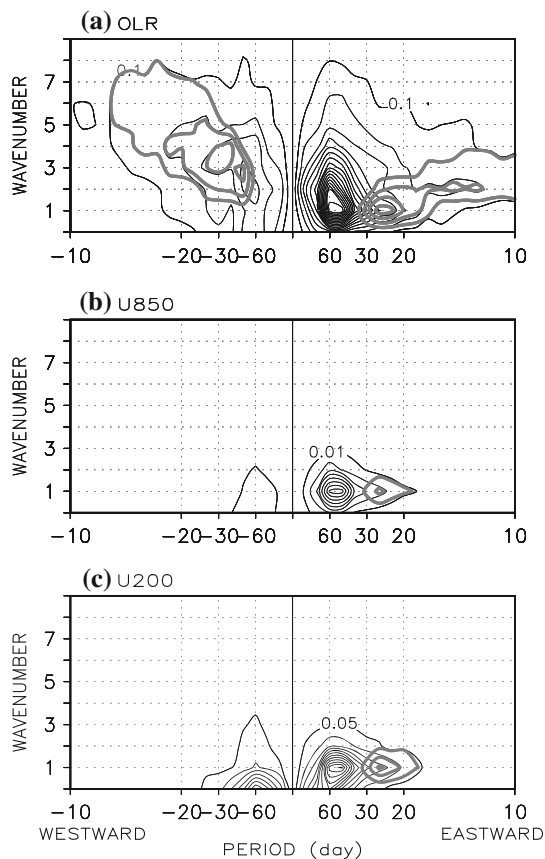


**Fig. 1** Frequency-wavenumber power spectra of raw daily anomalous data of WH04 during 1979–2012 for OLR (**a**  $0.1 \text{ W}^2 \text{ m}^{-4}$ ), U850 (**b**  $0.01 \text{ m}^2 \text{ s}^{-2}$ ), and U200 (**c**  $0.05 \text{ m}^2 \text{ s}^{-2}$ ), respectively. The *gray-thick curves* are for the equatorial Rossby and Kelvin waves (see text for the wave bands)

$0.03 \text{ m}^2 \text{ s}^{-2}$  at wavenumber 2 and less than  $0.01 \text{ m}^2 \text{ s}^{-2}$  at wavenumber 3 and beyond. Similarly, the U200 has power concentrated at wavenumber 1 and around 45–60 days with the central value of  $0.6 \text{ m}^2 \text{ s}^{-2}$ ; and the power diminishes rapidly at higher wavenumbers. The three fields clearly share the MJO spectra at wavenumbers 1–2 and over 30–100 day periods; the OLR has substantial power up to wavenumber 5.

Other signals are retained strongly in the raw anomalous data, including the westward propagating component of both the MJO and the equatorial Rossby waves and the eastward propagating equatorial Kelvin waves. The two convectively coupled waves were identified in the similarly anomalous data by regression (Roundy et al. 2009). For the OLR (Fig. 1a), the westward component longer than 50 days has power as large as  $0.3 \text{ W}^2 \text{ m}^{-4}$  and about 30 % of the eastward counterpart, which is sometimes classified as an MJO mode even though the signal has rarely been observed independently (Zhang 2005). The equatorial Rossby wave has maximum power of  $0.3 \text{ W}^2 \text{ m}^{-4}$  in 30–50 days and at wavenumbers 2–4 in westward

propagation. For the U850, the westward component much weaker than the eastward component and only reaches the first isopleth. For the U200, the westward component has power spectra as much as 50 % of the eastward counterpart in the zonal mean and around 60 days. This is why Slingo et al. (1996, 1999) selected the 200-hPa zonal-mean zonal wind to describe the MJO activity. For both the U850 and U200, the equatorial Rossby wave does not have power reaching the first isopleth and is thus considered weak. The equatorial Kelvin wave appears much weaker than the MJO and concentrated on 20–30 days in all three fields. Notably, WK99 classified the power spectra shorter than 30 days and at wavenumbers 1–4 in the eastward component as equatorial Kelvin waves, while some others classified the 20–30-day portion as the MJO (e.g., Maloney and Hartmann 1998; Slingo et al. 1996, 1999; Sperber 2003). We follow the classification of WK99 for a better comparison.

### 3.2 CEOF modes

Because the raw anomalous fields share the MJO as the primary signal, the CEOF analysis can be applied to the covariance matrix of the three fields to directly derive the closely coupled features in convection and circulation (WH04). Physically, each diagonal element of the matrix represents the normalized variance of the fields on a longitudinal grid. The total variance does not change after the CEOF analysis, but is reallocated among the eigenvalues. Thus, the sorted eigenvalues determine the order of importance of the corresponding eigenvectors to the total fields. An eigenvector is a CEOF mode that has a fixed pattern in space; the corresponding PC describes its time evolution. Spectral analysis indicates that the leading two CEOF modes share the predominant structure at zonal wavenumber 1 in the reconstructed anomalies, so the modes inevitably lack the power and the associated structures at wavenumbers 2–5. The higher-order CEOF modes can restore the lost power and structure, but they unavoidably introduce non-MJO variations. A balance between preserving the MJO structure and minimizing noise appears dependent on the proper number of CEOF modes.

Before seeking that number, the CEOF modes are compared in structure and explained variance. The leading pairs of modes for the three variables produced in this study have virtually identical structures to those in WH04. The higher-order modes each have more mixed structures at larger wavenumbers. Figure 2 presents these structures for modes 3–10 in the three fields before the global STDs were scaled back. The patterns are generally smooth and in wave form, and their wavenumbers become larger with larger mode number. A close inspection indicates that these

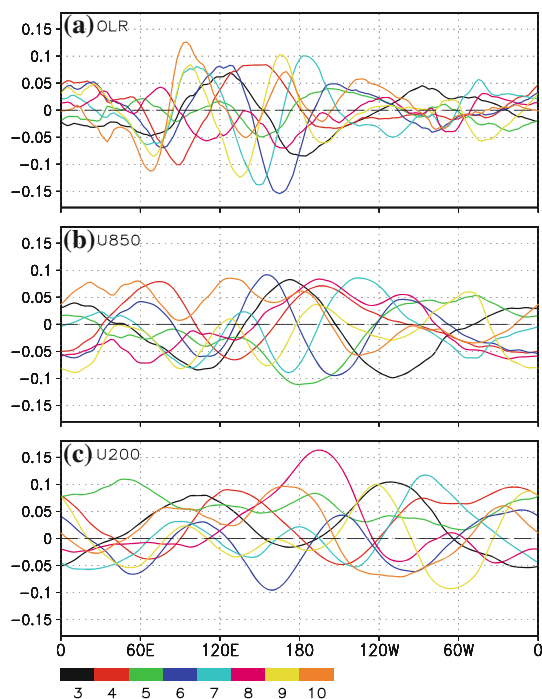


**Fig. 2** Structures of the CEOF modes 3–10 of **a** OLR, **b** U850, and **c** U200, respectively. Each color bar represents a mode with the number marked below

modes are dominant at wavenumbers 2–5, the OLR modes are more concentrated in the western Pacific than at other longitudes (Fig. 2a), the U850 modes are less concentrated (Fig. 2b), and the U200 the least concentrated but with large contribution to the zonal mean—for example, its mode 5 (shown in green) is positive everywhere. Nevertheless, their combined structure is of more interest than that of any individual mode to represent the MJO at wavenumbers 2–5. On the other hand, the explained variance does not converge to 0.01 % of the total until the 170th CEOF mode, because the three anomalous fields share large MJO power at wavenumber 1 and retain relatively strong variations at other bands (c.f. Fig. 1). Not surprisingly, the first two CEOF modes explain 13.6 and 12.2 %, respectively, of the variance—slightly more than those in WH04 due to the small difference in the regressed interannual variation. Notably, modes 3–10 explain 26.6 % of the total variance, more than the sum of the first two.

The accumulated percentage for each variable by the first 60 modes is further illustrated in Fig. 3, for which the variance was computed from the reconstructed anomalies. Since the zonal winds have power concentrated more at wavenumber 1 than does the OLR (c.f. Fig. 1), the first two modes contribute to the total variance by 35.1 % in the U850 and 31 % in the U200, much more than the 11.6 % in the OLR. As expected, more modes produce a larger contribution (Fig. 3a); for example, the first ten modes

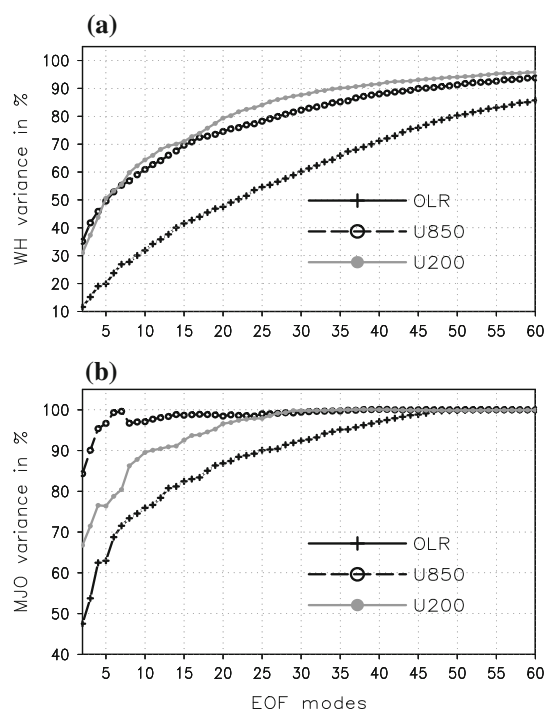


**Fig. 3** Accumulated variance in percentage of the reconstructed anomalies to the raw anomalous data (**a**) and of their MJO components to the total MJO (**b**). Shown are the first 60 out of 432 modes

**Table 1** Accumulated variance in percentage by the EOF modes to the raw daily anomalous data and the MJO components of the modes to the total MJO

	EOF1-2		EOF1-6		EOF1-10	
	RAW	MJO	RAW	MJO	RAW	MJO
OLR	11.6	47.5	23.8	68.8	31.9	75.9
U850	35.1	84.3	52.9	99.3	60.9	97.1
U200	31.0	66.8	53.2	78.8	64.4	89.5

contribute 31.9 % to the total in the OLR, 60.9 % in the U850, and 64.4 % in the U200 (Table 1). The accumulated percentage of MJO variance quickly approaches 100 % with the number of modes, indicating that the leading ten EOF modes contribute more to the total MJO variance than the rest, as similarly indicated in WH04 and shown in Fig. 3b and Table 1. The first two EOF modes contribute to the total MJO by 47.5 % in the OLR, 84.3 % in the U850, and 66.8 % in the U200. These large values explain why the RMM can generally detect the real-time MJO evolution in timing, phase, and amplitude. WH04 indicated that the third mode contributes to the MJO variance less prominently and the successive modes contribute even less (Fig. 3b). Thus, they used only the first two modes to represent the MJO. However, modes 3–10 can add 28.4 %

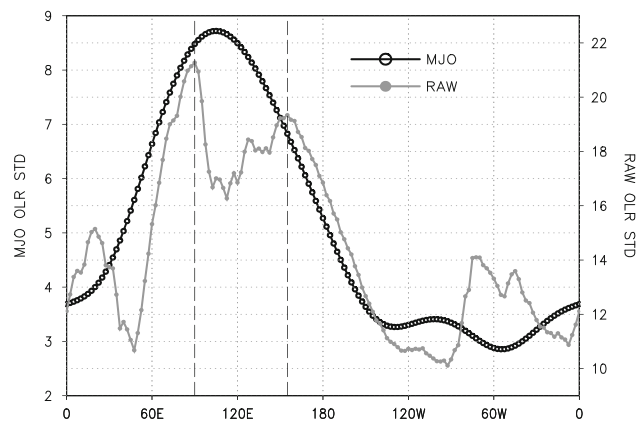


**Fig. 4** STD of the raw anomalous OLR (gray;  $W m^{-2}$ ; y-axis on right) and its MJO component (black; y-axis on left) during 1979–2012

to the power at the MJO band in the OLR, 12.8 % in the U850, and 22.7 % in the U200; they are essential to the MJO structure at higher wavenumbers. It is noteworthy that the first 6 CEOF modes have captured nearly 100 % of MJO variance in U850 and modes 7–10 modes reduce the variance slightly. This is because the CEOF analysis is applied to the raw—not filtered—data at MJO bands; the variance is computed from the reconstructed anomalies.

### 3.3 MJO STD and spectral structures

Next, the contribution of modes 3–10 to the MJO convection is demonstrated. As background, the total convective variability and MJO variance are large in the Eastern Hemisphere (e.g., Zhang 2005; Liu et al. 2005); their overall structure can be shown by the longitudinal distribution of STD in OLR. The STD of the raw anomalous OLR (gray in Fig. 4 and the y-axis on right) is above  $16 W m^{-2}$  between  $60^{\circ}E$  and  $180^{\circ}E$ , with one maximum of  $21.3 W m^{-2}$  at  $90^{\circ}E$  and another of  $19.3 W m^{-2}$  at  $155^{\circ}E$  (about 91 % of the first maximum) but below  $15 W m^{-2}$  in the rest of the tropics. A relative minimum of about  $16 W m^{-2}$  occurs at  $115^{\circ}E$ . The values of the two maxima will serve as a reference for comparison later. The STD at MJO bands has a single peak of  $8.7 W m^{-2}$  at  $105^{\circ}E$  (also referenced later) and is reduced to  $6.5 W m^{-2}$  at  $65^{\circ}E$  and  $155^{\circ}E$ . It decays to  $5.2 W m^{-2}$  at the dateline and below  $3.5 W m^{-2}$  in most of the Western Hemisphere. The relatively weak MJO in the central Pacific and Western Hemisphere makes its detection appealing.

The STD of the reconstructed anomalous OLR from the first two EOF modes (hereafter 2EOFs; gray-dashed in Fig. 5a) contributes to the total STD much more in the Eastern Hemisphere than in the Western Hemisphere. The proportion is over 40 % in  $70^{\circ}E$ – $150^{\circ}E$  with a maximum of

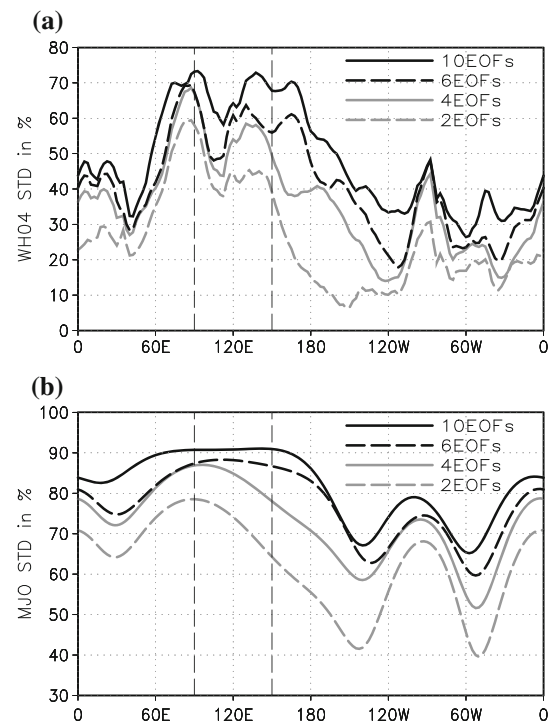


**Fig. 5** The STD in percentage to the total variance in Fig. 3 for the reconstructed OLR anomalies (a) and their MJO components (b) by the first two (gray-dashed), four (gray-solid), six (black-dashed) and ten (black-solid) EOF modes

about 60 % at  $85^{\circ}E$ . From  $170^{\circ}E$  eastward, including the Western Hemisphere, the contribution is less than 20 % except for a peak of 30 % near  $30^{\circ}W$ . Given that the total STD is strong in the Eastern Hemisphere (c.f. Fig. 4) and that the anomalous OLR contains primarily MJO signals (c.f. Fig. 1), the 2EOFs anomaly captures the distribution of OLR at MJO bands reasonably well. However, a close inspection indicates that the contribution at  $155^{\circ}E$  is only 40 %, about 20 % less than that at  $90^{\circ}E$ , making the STD 50 % smaller than the baseline MJO. The proportion further reduces to 20 % near  $170^{\circ}E$ . Similarly, the 2EOFs component of the MJO bands (gray-dashed in Fig. 5b) has a single maximum contribution of 78 % at  $90^{\circ}E$ , making the maximum STD of  $6.7 W m^{-2}$  at  $100^{\circ}E$  (3rd row in Table 3), about  $5^{\circ}$  westward to that of the baseline (c.f. Fig. 4). Moving eastward, the percentage drops to 65 % at  $155^{\circ}E$ , corresponding to the OLR of  $4.25 W m^{-2}$  and about 63 % of the maximum. The distribution suggests that the 2EOFs tend to predict weaker amplitude of OLR at MJO bands in the western Pacific.

Such low allocation of STD in the western Pacific is caused systematically by the structures of the first two EOF modes that dominate at zonal wavenumber 1; these values decay rapidly in the western Pacific. Spectral analysis also reveals this power dominance in the reconstructed

**Table 2** STD featured values and locations for the raw daily anomalous data

	Max value	Longitude location of max	Value at 155°E	Percentage of value at 155°E to max
RAW	21.27	90	19.34	90.91
2EOFs	12.57	87.5	6.37	50.67
4EOFs	14.50	87.5	8.66	59.71
6EOFs	14.67	87.5	11.20	76.33
8EOFs	14.72	87.5	13.01	88.38
10EOFs	15.56	90	13.10	84.22

**Table 3** Same as Table 2 but for the MJO

	Max value	Longitude location of max	Value at 155°E	Percentage of value at 155°E to max
WH04	8.68	105	6.80	78.33
2EOFs	6.74	100	4.25	63.15
4EOFs	7.53	102.5	5.22	69.29
6EOFs	7.66	105	5.87	76.64
8EOFs	7.88	107.5	6.09	77.23
10EOFs	7.87	105	6.17	78.31

anomalies (not shown). Including more CEOF modes improves the representation, as shown by the rest of the curves in Fig. 5. Modes 3–4 increase the contributions of both the reconstructed OLR and its component at MJO bands nearly everywhere (gray-solid). Modes 5–6 (black-dashed) contribute even more, particularly in the region at 90–155°E, which brings the percentage at MJO bands closer with a difference of less than 7 % in the range of 60–170°E. The 10EOFs (black-solid) retains the variance structure sufficiently; the percentage is 60–72 % in 60–180°E with three nearly identical maxima at 90°E, 135°E and 170°E, and it decreases to 30–45 % in the Western Hemisphere. Notably, they comprise nearly 90 % of the total STD at MJO bands and within 1 % difference in 60–170°E, which literally preserves the shape of the baseline MJO in that wide region (Fig. 5b). The modes also enhance the contribution of the MJO in the Western Hemisphere to 65–85 %. Tables 2 and 3 list the maximum values and their locations and the values at 155°E for each case; they also clearly show that the 10EOF-based anomalies agree well with the raw anomalous OLR and its component at the MJO bands (last rows).

The added variance by the modes 3–10 includes both MJO and other variations, probably as noise. To estimate the partitions, the difference between the Fourier power spectra of the anomalies reconstructed by the first 10 and 2 CEOF modes was computed, shown in Fig. 6. Overall, the

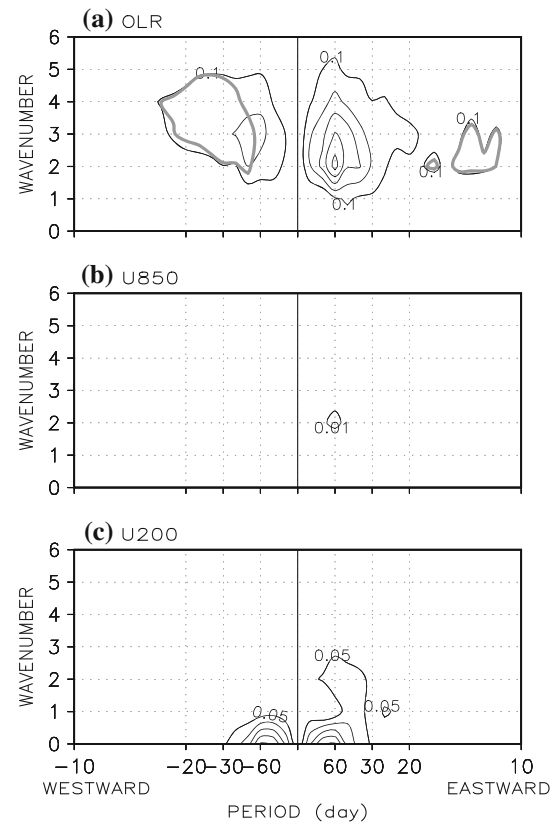


**Fig. 6** Difference of power spectra between the reconstructed anomalies by the first 10 and 2 EOF modes for the anomalous OLR (a  $0.1 \text{ W}^2 \text{ m}^{-4}$ ), U850 (b  $0.01 \text{ m}^2 \text{ s}^{-2}$ ), and U200 (c  $0.05 \text{ m}^2 \text{ s}^{-2}$ ), respectively. The thick-gray curves are for the ER and Kelvin waves

additional power is much larger for the MJO at eastward wavenumbers 2–5 and over 30–100 day periods than for other variations that are manifested as the equatorial Kelvin and Rossby waves (gray-thick curves in Fig. 6), indicating a high signal-to-noise ratio. Specifically, the OLR adds  $0.5 \text{ W}^2 \text{ m}^{-4}$  at wavenumber 2 and around 60 days (Fig. 6a), about 40 % of the total at this band, and about 50 % of the total at wavenumbers 3–5 (c.f. Fig. 1), but only  $0.1 \text{ W}^2 \text{ m}^{-4}$  at wavenumber 1, indicating where the 2EOFs dominate. The U850 (Fig. 6b) contributes 10 % more at wavenumber 2, where the U200 (Fig. 6c) adds 15 % more. Interestingly, modes 3–10 include notably more power in the zonal-mean U200. The dynamical relation behind this is unclear, since all the modes are of mathematical origin. The 10EOFs increases the spectra of the ER and Kelvin waves up to 1 isopleth in Fig. 6, much smaller than the MJO, particularly in the OLR. Compared with Fig. 1, the modes add 25 % more power to the waves that are also relatively stronger in the OLR than in the U850 and U200. The enhanced ER and Kelvin waves partially contribute to the MJO evolution, as shown in the next subsection. It is noteworthy that the 2EOFs also include the westward

component of the MJO at wavenumber 1 and of  $0.2 \text{ W m}^{-2}$  (not shown), and the 10 EOFs expand this component to wavenumbers 2–5. The CEOF modes beyond 10 introduce more power in small-scale variations but less in the MJO; they may be discarded. Because their MJO component has a structure nearly identical to the MJO in the raw data from the central Indian Ocean to the western Pacific (c.f. Fig. 5b), and the additional power spectra have a high signal-to-noise ratio of MJO, the 10 CEOF modes are satisfactory to represent the baseline MJO.

### 3.4 Three MJO events

#### 3.4.1 Hovmöller diagrams

The Hovmöller diagrams of three MJO events with distinct structures demonstrate how the CEOF modes 3–10 combine to retain the MJO structure and how the included equatorial Rossby and Kelvin waves incorporate partially with the MJO evolution. Since at wavenumbers 2–5 the modes add the most power to the OLR, with less going to the U850 and the least to the U200, the diagrams for the OLR and U850 are displayed. The first two MJO events occurred during the TOGA-COARE and have been investigated extensively (e.g., Yanai et al. 2000; Straub 2013) and the third occurred in spring 2012 and partially observed by the Dynamics of the Madden–Julian Oscillation field program (DYNAMO; Zhang et al. 2013). These events can be identified visually in the raw anomalous fields, mixed in with rich small-scale structures (Figs. 7a, 9a). The filtered OLR and U850 at MJO bands provide the lifetime and magnitude for each event (Figs. 7b, 9b), in spite of the caution that should be taken with the initiation in time (Straub 2013). The first event starts near 25 November 1992 with the filtered OLR smaller than  $-5 \text{ W m}^{-2}$  at  $95^\circ\text{E}$  (Fig. 7b). It develops and strengthens in the western Pacific with a center less than  $-25 \text{ W m}^{-2}$ . The event ends at  $150^\circ\text{W}$  around 11 January 1993. Correspondingly, the U850 is westerly and slightly lags the OLR in the western Pacific, which is a classic quadrature structure of MJO dynamics (Zhang 2005). The reconstructed OLR by the first two EOF modes detects this event with a rather small amplitude in the western Pacific (Figs. 7c, 8a) that is less than half of the MJO strength in the raw data (shading in Fig. 7b), while the reconstructed U850 appears stronger (contour in Fig. 7b). The anomalies reconstructed by the first 10 modes (Figs. 7d, 8d) clearly represent this robust event with complete evolution, correct lifetime, and central value near the dateline that are consistent with the results of Yanai et al. (2000). Notably, the first event has a convective center near  $170^\circ\text{E}$  and a U850 center slightly westward, which is a typical feature in the

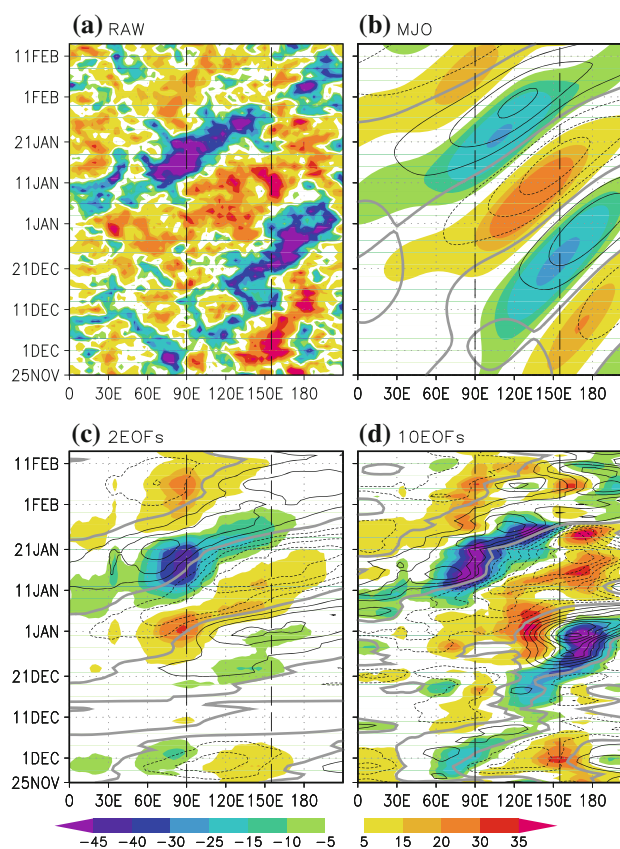


**Fig. 7** Hovmöller diagrams for the raw anomalous OLR of WH04 (a), the filtered anomalies of WH04 at MJO bands (b), the reconstructed anomalies from the first 2 (c) and 10 (d) EOF modes during 25 November 1992–14 February 1993. The color shadings are for the OLR and the contours for U850 with interval of  $1 \text{ m s}^{-1}$  and the gray-thick as 0

composite analysis (Sperber 2003). The structure suggests that the first MJO event is dominant at wavenumbers 2–5.

The second MJO event (Fig. 7b; Straub 2013) is initiated near Africa in the western Indian Ocean in the beginning of 1993. It develops in the eastern Indian Ocean, matures near  $115^\circ\text{E}$ , weakens slightly over the Maritime Continent and at  $155^\circ\text{E}$ , and decays rapidly eastward. The 2 EOF-based anomalies (Fig. 7c) follow the initiation and development in the Indian Ocean, but reach their maximum at  $90^\circ\text{E}$  which is west of the baseline's center. Thereafter they weaken substantially eastward in both OLR and U850. The lost amplitude in the western Pacific can be restored again by modes 3–10. During this event, the MJO, equatorial Kelvin, and Rossby waves in the anomalies reconstructed by the first 2 and 10 EOF modes are shown in Fig. 8. Clearly the 2 EOF-based MJO anomalies are very weak, particularly in the western Pacific, while the 10 EOF-based (Fig. 8d) agree well with the baseline (Fig. 7b). The Kelvin and Rossby waves are also enhanced in the 10 EOFs and partly embedded in the MJO evolutions to form the closed centers for the two events (Fig. 7c, d).



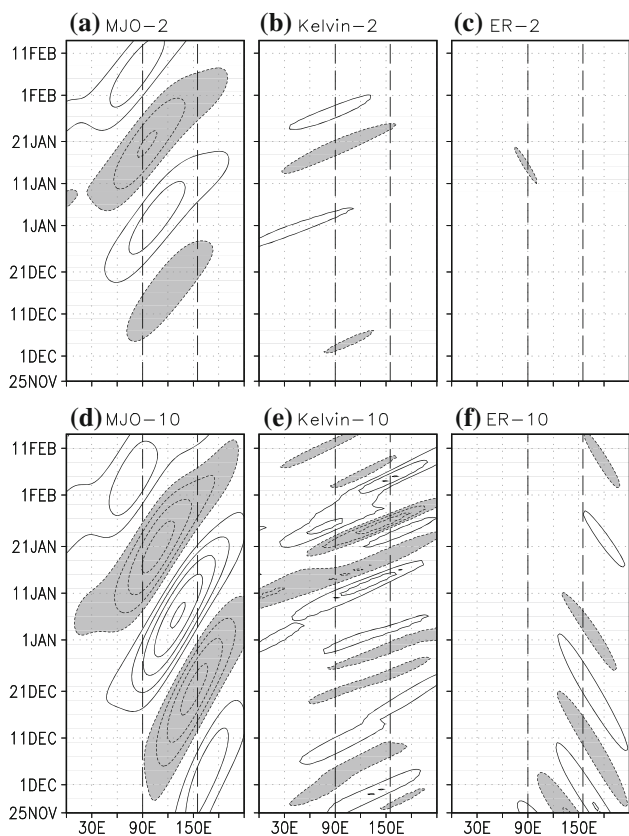


**Fig. 8** Hovmöller diagrams for the MJO (a, d), equatorial Kelvin waves (b, e), and ER waves (c, f) in the reconstructed anomalous OLR from the first 2 (a–c) and 10 (d–f) EOF modes during 25 November 1992–14 February 1993. The contour interval is  $5 \text{ W m}^{-2}$  and values at and smaller than  $-5 \text{ W m}^{-2}$  are shaded in light gray

The third MJO event (Fig. 9b) covers 16 February–15 April 2012 and has a structure similar to that of a composite MJO (Maloney and Hartmann 1998). It starts and develops in the Indian Ocean, matures near  $100\text{--}120^\circ\text{E}$ , and remains strong eastward to the dateline. The 2EOF based anomalies (Fig. 9c) still specify its center at  $90^\circ\text{E}$ , while the amplitude decays rapidly eastward such that the magnitude and timing in the western Pacific agree less well with the reference condition. The amplitude is mostly restored in the anomalies reconstructed by the first 10 EOF modes over the western Pacific (Fig. 9d). For the MJO, the 2EOFs (Fig. 10a) has about half of the magnitude in the raw data (c.f. Fig. 7b), while the 10EOFs (Fig. 10d) contributes nearly 90 % to the total from  $70^\circ\text{E}$  to the dateline, consistent with the STD analysis (c.f. Fig. 5b). The enhanced Kelvin and Rossby waves (Fig. 10b, e) are embedded partially in and move with the MJO and add to form the three closed maxima of OLR and U850 (Fig. 9d), suggesting their significance to the MJO dynamics (e.g., Wang 1988; Zhang 2005). The evolution of the three distinct MJO events on the Hovmöller diagrams indicates that

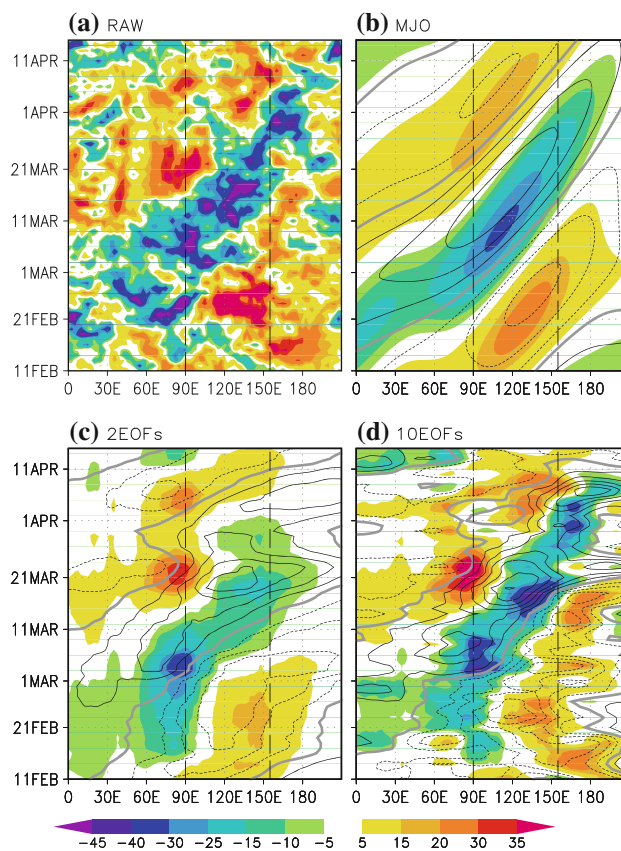


**Fig. 9** Same as Fig. 7 but during 1 February–15 April 2012

the first 10 CEOF modes can retain the MJO structure sufficiently and the noise is primarily from the equatorial Kelvin and Rossby waves.

### 3.4.2 Longitudinal STD for MJO magnitude

The amplitude of the RMMs  $(\text{RMM1}^2 + \text{RMM2}^2)^{1/2}$ , was adopted after WH04 to represent the daily MJO magnitude without much explanation of its physical basis. Since each RMM is the normalized version of the PC that describes the time evolution of the corresponding CEOF mode, the RMM amplitude can be associated with the longitudinal STD of the reconstructed anomalies as demonstrated below.

On a given day, the  $i$ th reconstructed component  $a_i$  ( $1 \leq n < 432$ ) in vector form of the combined anomalous OLR, U850, and U200 (each normalized by their global standard deviation) can be expressed as

$$a_i = PC_i \times CEOF_i,$$

where  $PC_i$  is a single value. The reconstructed anomalies from the first  $n$  ( $1 \leq n < 432$ ) CEOF modes  $a_{1-n}$  simply add up the  $n$  components at each longitude. Thus, the longitudinal STD  $v_{1-n}$  has the form

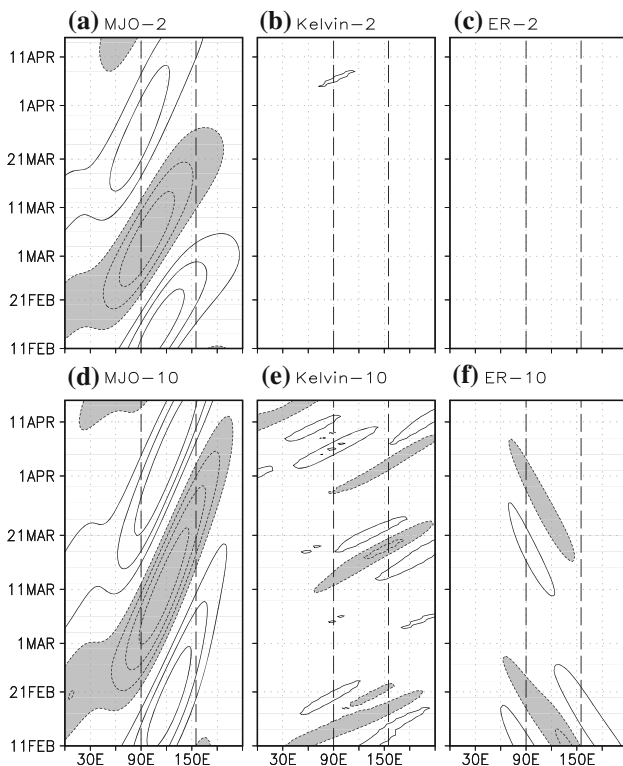


**Fig. 10** Same as Fig. 8 but during 1 February–15 April 2012

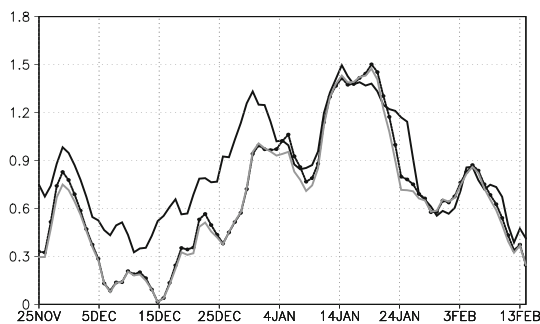


**Fig. 11** Longitudinal STD of the reconstructed anomalous data from the first two (black-dotted) and ten (black) CEFOF modes during 25 November 1992–15 February 1993. The reconstruction was made by projecting the anomalous OLR, U850 and U200 being scaled by their globally averaged STD onto the CEFOF modes as a whole. The RMM amplitude  $(RMM1^2 + RMM2^2)^{1/2}$  is displayed in gray. Only the y-axis for the 10EFOF-based longitudinal STD is displayed and those for the 2EFOF-based and the RMM amplitude are omitted

$$v_{1-n} = \sqrt{\frac{1}{431} \sum_{j=1}^{432} (a_{1-n}^j - \overline{a_{1-n}})^2},$$

where the overbar represents the average in longitude. If  $\overline{a_{1-n}} = 0$ , the above expression for  $v_{1-n}$  can be rewritten as

$$v_{1-n} = \sqrt{\sum_{i=1}^n PC_i^2 \left[ \frac{1}{431} \sum_{j=1}^{432} (CEOF_i^j)^2 \right]},$$

because  $PC_i$  does not change in longitude. Only when the longitudinal averages of the CEFOF patterns (eigenvectors) are zero and the variances of the patterns (the second summation under the radical sign) are identical, would the RMM-like amplitude be accurately scaled to  $v_{1-n}$ . Calculations indicate that both  $\overline{a_{1-n}}$  and  $\overline{CEOF_i}$  can be small but rarely zero and that different longitudinal variance exists in the CEFOF patterns. Thus some RMM amplitude can be scaled slightly below the longitudinal STD of the reconstructed anomalies from the first two CEFOF modes, while the difference is accumulated and can become much larger and noisier for the first 10 modes. The longitudinal STD indicates below that the first ten CEFOF modes can detect the MJO phases in the western Pacific better than the first two modes.

The longitudinal STD for the two MJO events during the TOGA-COARE is displayed in Fig. 11. Overall, the longitudinal STD of the first two CEFOF modes (black-dotted) scales very well to the RMM amplitude (gray); they are nearly identical at some locations, while the STD is slightly above the RMM amplitude at the rest, as discussed above. By scaling the peaks of the RMM amplitude and the longitudinal STDs of the anomalies from the first 2 (black-dotted) and 10 (black) CEFOF modes for the second event to nearly identical levels, the first event represented by the 10EFOF-based longitudinal STD (black) stands out from the other curves during each day of its lifecycle. In particular, its peak is much closer to that of the second event, which indicates substantial improvement and agrees well with that on the Hovmöller diagrams (c.f. Fig. 7). A similar improvement of smaller magnitude also occurs during the last peak of the third event in spring 2012 (not shown), suggesting that the longitudinal STD of the first 10 modes has monitored the MJO evolutions in the western Pacific more accurately than that of the first two.

#### 4 Summary and discussion

The leading two CEFOF modes of daily anomalous OLR, U850 and U200, which formulate the RMM index of WH04, can represent the evolution of MJO in phase and timing (WH04). However, the two modes allocate more power at MJO bands in the eastern Indian Ocean than in the western Pacific in both the anomalous data and their MJO components, which induces notably smaller amplitude—particularly of the OLR in the western Pacific—than the MJO in the raw data, as demonstrated by the STD analysis and the Hovmöller diagrams of the three MJO events. Such incomplete MJO structure is caused by the predominantly wavenumber-1 configuration of the leading two CEFOF modes, while the MJO power spectra at wavenumbers 2–5

are substantially underestimated. The CEOF modes 3–10 restore this part of power effectively, which increases the amplitude of the OLR and U850 in the western Pacific and makes the MJO evolution more complete on the Hovmöller diagrams. These additional modes can also improve the longitudinal STD of the reconstructed anomalous data to detect the MJO evolutions in the western Pacific better than that of the first two CEOF modes only, after the RMM amplitude is demonstrated as a conditional simplification of the longitudinal STD.

Modes 3–10 include more power spectra of the equatorial Rossby and Kelvin waves in the OLR and U850 as well. Roundy et al. (2009) indicated by regression that these waves occur in accordance with the MJO under the RMM framework, supporting their importance in the MJO's development and evolution (e.g., Wang 1988; Wang and Rui 1990), and despite their occurrence can be independent of MJO (Roundy 2012a). The power spectra at low zonal wavenumbers and over 20–30 days of eastward propagation are classified as the equatorial Kelvin waves in this study, though they can also contain some MJO signals (e.g., Maloney and Hartmann 1998; Slingo et al. 1996, 1999; Sperber 2003; Roundy 2012a, b); these bands can be an essential transition between the equatorial Kelvin waves and the MJO. To include these waves in the reconstructed anomalies adds useful information to the MJO evolution.

It is noteworthy that the RMM phase diagram (WH04), while substantially simplifying the detection of MJO evolution, cannot be revised satisfactorily with the additional CEOF modes. This simple but effective phase map alone, however, can falsely identify an MJO event and its phases (Straub 2013). It is usually combined with the Hovmöller diagrams of the reconstructed OLR and U850 and with the RMM amplitude for real-time applications (WH04). The results of this study can make the combination more robust by including the 10 CEOF modes in the Hovmöller diagrams and replacing the RMM-like amplitude with the longitudinal STD of the 10 CEOF components. In addition, because modes 3–10 add the MJO signal primarily at zonal wavenumbers 2–5 and over the western Pacific, the improvement appears less helpful in describing the MJO initiation (Straub 2013) that occurs particularly in the Indian Ocean.

Similar results to this study have been obtained by using the anomalous data subject to conventional band-pass filtering in 20–80 or 30–80 day periods, suggesting that the additional CEOF modes can be useful for validating the MJO simulations and operational forecast by numerical models.

**Acknowledgments** This research is partially supported by the Office of Sciences of the U.S. Department of Energy to Stony Brook

University. Interpolated OLR data and the zonal winds are provided by the NOAA/OAR/ESRL PSD, Boulder, Colorado, USA, from their Web site at <http://www.esrl.noaa.gov/psd/>. The manuscript has benefited substantially from the constructive comments made by the anonymous reviewers. Useful comments also came from Drs. Melanie A. Wolfe Pitt and Christopher Wolfe.

## References

- Drosowsky W, Chambers LE (2001) Near-global sea surface temperature anomalies as predictors of Australian seasonal rainfall. *J Clim* 14:1677–1687
- Gottschalck J et al (2010) A framework for assessing operational Madden–Julian oscillation forecasts. *Bull Am Meteorol Soc* 91:1247–1258
- Hendon HH, Salby ML (1994) The life cycle of the Madden–Julian oscillation. *J Atmos Sci* 51:2225–2237
- Hendon HH, Zhang C, Glick JG (1999) Interannual variation of the Madden–Julian oscillation during Austral summer. *J Clim* 12:2538–2550
- Kalnay E et al (1996) The NCEP/NCAR 40-year reanalysis project. *Bull Am Meteorol Soc* 77:437–470
- Kiladis GN, Straub KH, Haertel PT (2005) Zonal and vertical structure of the Madden–Julian oscillation. *J Atmos Sci* 62:2790–2809
- Kim D et al (2009) Application of MJO simulation diagnostics to climate models. *J Clim* 22:6413–6436
- Knutson TR, Weickmann KM (1987) 30–60 day atmospheric oscillations: composite life cycles of convection and circulation anomalies. *Mon Weather Rev* 115:1407–1436
- Lau KM, Chan PH (1985) Aspects of the 40–50 day oscillation during the northern winter as inferred from outgoing long-wave radiation. *Mon Weather Rev* 113:1889–1909
- Liebmann B, Smith CA (1996) Description of a complete (interpolated) outgoing longwave radiation dataset. *Bull Am Meteorol Soc* 77:1275–1277
- Liu P, Wang B, Sperber KR, Li T, Meehl GA (2005) MJO in the NCAR CAM2 with the Tiedtke convective scheme. *J Clim* 18:3007–3020
- Liu P et al (2009) An MJO simulated by the NICAM at 14-km and 7-km resolutions. *Mon Weather Rev* 137:3254–3268
- Madden RA, Julian PR (1971) Detection of a 40–50 day oscillation in the zonal wind in the tropical Pacific. *J Atmos Sci* 28:702–708
- Madden RA, Julian PR (1972) Description of global-scale circulation cells in the Tropics with a 40–50 day period. *J Atmos Sci* 29:1109–1123
- Maloney ED, Hartmann DL (1998) Frictional moisture convergence in a composite life cycle of the Madden–Julian oscillation. *J Clim* 11:2387–2403
- Rayner NA et al (2003) Global analyses of sea surface temperature, sea ice, and night marine air temperature since the late nineteenth century. *J Geophys Res* 108:4407. doi:10.1029/2002JD002670
- Roundy PE (2012a) The spectrum of convectively coupled Kelvin waves and the Madden–Julian oscillation in regions of low-level easterly and westerly background flow. *J Atmos Sci* 69:2107–2111
- Roundy PE (2012b) Observed structure of convectively coupled waves as a function of equivalent depth: Kelvin waves and the Madden–Julian oscillation. *J Atmos Sci* 69:2097–2106
- Roundy PE, Schreck CJ III, Janiga MA (2009) Contributions of convectively coupled equatorial Rossby waves and Kelvin waves to the real-time multivariate MJO indices. *Mon Weather Rev* 137:469–478

- Slingo JM et al (1996) Intraseasonal oscillations in 15 atmospheric general circulation models: results from an AMIP diagnostic subproject. *Clim Dyn* 12:325–357
- Slingo JM, Powell DP, Sperber KR, Nortley F (1999) On the predictability of the interannual behaviour of the Madden–Julian oscillation and its relationship with El Niño. *Q J R Meteorol Soc* 125:583–609
- Sperber KR (2003) Propagation and the vertical structure of the Madden–Julian oscillation. *Mon Weather Rev* 131:3018–3037
- Straub KH (2013) MJO initiation in the real-time multivariate MJO index. *J Clim* 26:1130–1151
- The NCAR command language (version 6.1.1) [software], 2013. UCAR/NCAR/CISL/VETS, Boulder, CO. <http://dx.doi.org/10.5065/D6WD3XH5>
- Wang B (1988) Dynamics of tropical low frequency waves: an analysis of moist Kelvin waves. *J Atmos Sci* 45:2051–2065
- Wang B, Rui H (1990) Dynamics of the coupled moist Kelvin–Rossby wave on an equatorial  $\beta$ -plane. *J Atmos Sci* 47:397–413
- Webster PJ, Lukas R (1992) TOGA COARE: the coupled ocean–atmosphere response experiment. *Bull Am Meteorol Soc* 73:1377–1416
- Wheeler M, Hendon HH (2004) An all-season real-time multivariate MJO index: development of an index for monitoring and prediction. *Mon Weather Rev* 132:1917–1932
- Wheeler M, Kiladis GN (1999) Convectively coupled equatorial waves: analysis of clouds and temperature in the wavenumber–frequency domain. *J Atmos Sci* 56:374–399
- Yanai M, Chen B, Tung WW (2000) The Madden–Julian oscillation observed during the TOGA COARE IOP: global view. *J Atmos Sci* 57:2374–2396
- Zhang C (2005) Madden–Julian oscillation. *Rev Geophys* 43:RG2003. doi:10.1029/2004RG000158
- Zhang C, Gottschalck J, Maloney ED, Moncrieff MW, Vitart F, Waliser DE, Wang B, Wheeler MC (2013) Cracking the MJO nut. *Geophys Res Lett* 40:1223–1230